Structural and Electrochemical Studies of Novel Bis(μ-methoxo)diiron complexes: Observation of $Fe^{III}Fe^{IV}$ and $Fe^{IV}Fe^{IV}$ States Resonating with Phenoxyl Radicals

Hirohiko Houjou,*[a, d] Masatoshi Kanesato,[a] Kazuhisa Hiratani,[a, b] and Dominique Mandon[c]

Abstract: Novel diiron complexes with an $Fe_2(\mu\text{-}OMe)_2$ core were studied as models of the active site of nonheme iron-containing enzymes. X-ray crystal structures of the complexes showed the existence of two types of ligand folding—parallel and twisted—both of which have four virtually equivalent phenolato groups sticking out from the Fe_2O_2 rhombic plane. Cyclic voltammetry measurements revealed two or more distinct redox waves in a region of relatively high potential, in addition to known Fe^{II}/Fe^{III} redox waves in a region of lower potential. These new peaks were assigned to the high-valence state of iron atoms, that is, Fe^{III}-Fe^{IV} and $Fe^{IV}Fe^{IV}$, resonating with the phenoxyl radical(s). The split width of the redox waves ranged from 0.14 to 0.20 eV, which may be a measure of the electronic interaction of the phenolate groups through the $Fe_2(\mu\text{-}OMe)_2$ core.

Keywords: cyclic voltammetry · iron · metalloenzymes · phenoxy radicals · Schiff bases

Introduction

Dinuclear iron complexes with a $Fe_2(\mu\text{-}O)_2$ "diamond core" have been extensively studied in terms of their relevance to dioxygen activation in nonheme iron-containing enzymes, such as methane monooxygenase (MMO), ribonucleotide reductase (RNR), and stearoyl-ACP Δ^9-desaturase.[1,2] These proteins function through a sequential multistep change in the oxidation state of the iron-containing active site; in particular, the formation of a high-valence iron–oxo intermediate as a key step in the oxidative catalytic cycle has attracted much attention. For example, intermediate Q of MMO was identified as having an $Fe^{IV}Fe^{IV}$ state, whereas intermediate X of the R2 subunit of RNR has an $Fe^{III}Fe^{IV}$ mixed valence state.[1,2] To elucidate the structural and functional aspects of these intermediates, several molecular models have been proposed by using synthetic complexes[3–9] and by the DFT computational approach.[7,10,11] Although only one example of an $Fe^{III}Fe^{IV}$ complex has been crystallographically characterized,[3] there is spectroscopic evidence for the formation of a high-valence diiron state through chemical or electrochemical oxidation.[4–8] Because of their low stability, the study of these high-valence species normally requires low-temperature analyses.

The development of new ligands that can stabilize the high-valence diiron diamond core will contribute to the further understanding of this kind of chemistry. Several types of diiron complexes with $Fe_2(\mu\text{-}OH)$,[12–14] $Fe_2(\mu\text{-}OR)$,[15–19] or $Fe_2(\mu\text{-}RCO_2)$[20,21] bridging moieties (R = alkyl or aryl) have been reported; however, these were mainly described from the point of view of their crystal structures and magnetic properties, particularly the antiferromagnetic interaction between the two iron atoms. Although there are some descriptions of electrochemistry, the main interest has been focused on the $Fe^{II}Fe^{III}$ mixed valence state. More generally, there are only few studies devoted to the electrochemical properties of diiron cores in high-valence states.

[a] Dr. H. Houjou, Dr. M. Kanesato, Prof. K. Hiratani
Nanoarchitectonics Research Center
National Institute of Advanced Industrial Science and Technology (AIST)
Tsukuba Central 4, 1-1-1 Higashi, Tsukuba
Ibaraki 305-8562 (Japan)
E-mail: houjou@iis.u-tokyo.ac.jp

[b] Prof. K. Hiratani
Department of Applied Chemistry, Utsunomiya University
7-1-2 Youtou, Utsunomiya 321-8585 (Japan)

[c] Prof. D. Mandon
Laboratoire de Chimie Biomimétique des Métaux de Transition
UMR CNRS No. 7513, Université Louis Pasteur
Institut Le Bel, 4 rue Blaise Pascal
67070 Strasbourg Cedex (France)

[d] Dr. H. Houjou
Present address: Institute of Industrial Science
University of Tokyo, 4-6-1 Komaba, Meguro
Tokyo 153-8505 (Japan)
Fax: (+81) 3-5452-6366

DOI: 10.1002/chem.200400114

The question of thermodynamic stability of the diiron site may make it difficult to get clean measurements. Additional difficulties in studying high-valence states may occur because the redox potential of the Fe^{III}/Fe^{IV} couple occasionally overlaps that of the ligands, and this often gives rise to irreversible oxidation of the complex. Thus, stable diiron complexes with structures close to the diamond core unit need to be obtained. In the past, we have developed new Schiff base ligands containing a 2-methylenepropane-1,3-diyl (the so-called isobutenylene) chain,[22,23] and have succeeded in synthesizing dinuclear complexes of Ti^{IV}, Y^{III}, Ni^{II}, and Cu^{II}.[24–26] Among these complexes, we found that the Ti^{IV} one has a $Ti_2(\mu\text{-}O)_2$ core surrounded with an assembled pair of the ligands.[24] This finding suggested a possible access route to an isostructural complex with a diiron core, by using the same ligand. Furthermore, it is expected that the incorporation of a redox-active ligand, such as the phenolato group (i.e., a noninnocent ligand),[27] stabilizes the high valence state of the complex by through-resonance interactions between the oxidation states of the metal and the ligands. Thus, measurements could be perfomed at ambient temperatures. In this article, we describe the synthesis and electrochemical properties of novel bis(μ-methoxo)-diiron complexes, and make an initial attempt to elucidate the electrochemical character of the $Fe_2(\mu\text{-}O)_2$ diamond core.

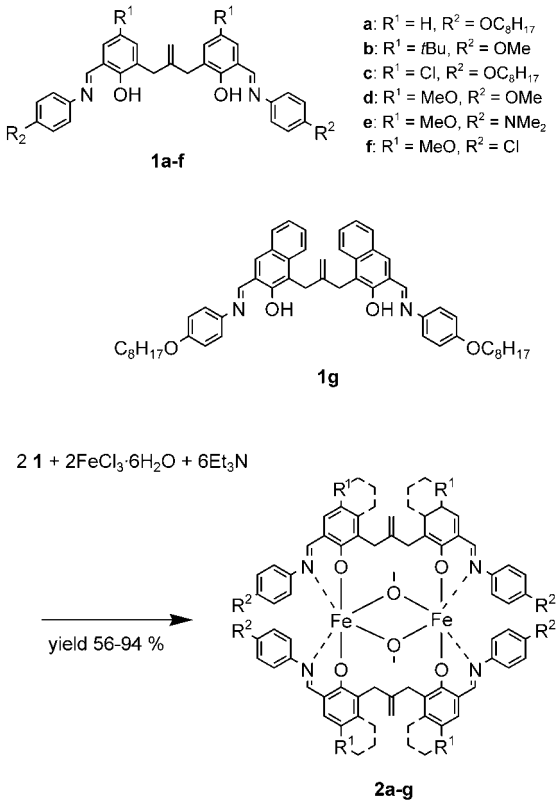

Scheme 1. Synthesis of the bis(μ-methoxo)diiron complexes.

Results and Discussion

Structure of the diiron(III) complexes: The reaction of the ligands **1a–g** with iron(III) chloride hexahydrate in the presence of methanol afforded the corresponding bis(μ-methoxo)diiron complexes **2a–g** with good yields (Scheme 1). The complexes **2b**, **2c**, and **2d** should demonstrate the electronic effects of the substituents of the phenolate group, whereas **2d**, **2e**, and **2f** should clarify the role of those present on the phenylimine group. The complex **2g** has naphthalene rings instead of benzene rings. The octyloxy groups in **2a**, **2c**, and **2g** were introduced for the sake of solubility.

Figure 1 shows the crystal structure of **2b**, which has *tert*-butyl groups on the phenolate moieties. The strands of the two ligand moieties are folded without twisting, and are wrapped around two iron atoms. The two phenolic oxygen atoms from one ligand are bound to two different iron atoms. The two imine nitrogen atoms from one ligand are also bound to two different iron atoms. The two iron atoms are connected by two methoxo bridging ligands. Consequently, each iron atom has an octahedral geometry with N_2O_4-type hexacoordination (Figure 2). The whole molecule has C_i symmetry (virtually C_{2h} symmetry with the C_2 axis coincident with the Fe–Fe vector), and the Fe_2O_2 rhombus has a point of symmetry. This structure is quite similar to that of the dinuclear Ti^{IV} complex with respect to the M_2O_2 rhombic core and the ligand folding.[24] The structure shown in Figure 1 is that of one of the two independent molecules in the unit cell; these have essentially identical structures except for the torsional direction of the methoxy groups on

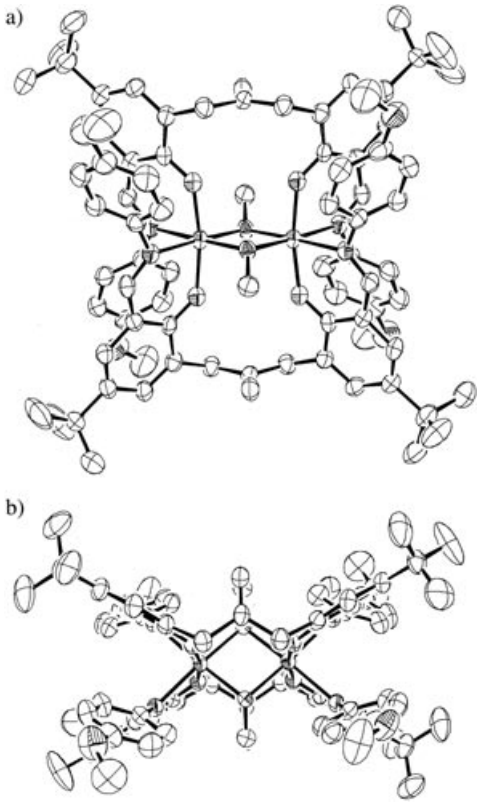

Figure 1. The crystal structure of **2b**-I (one of the two crystallographically independent molecules). Views from the directions a) nearly parallel and b) nearly perpendicular to the Fe_2O_2 rhombic plane.

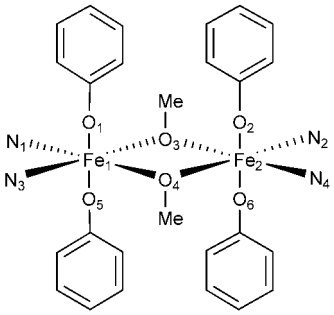

Figure 2. The $Fe_2(\mu\text{-}MeO)_2$ core structure studied in this paper. The numbering system used in Table 1 is shown.

the phenylimine moiety. The detailed geometrical parameters are given in Table 1.

Figure 3 shows the crystal structure of **2e**, with methoxy groups present on the phenolate moieties and dimethylamino groups on the phenylimine moieties. By contrast to what

Table 1. Selected bond lengths [Å] and angles [°] of the diiron complexes.[a]

	2b-I	**2b**-II	**2e**	**2f**
Fe1–N1	2.203(5)	2.205(5)	2.133(14)	2.189(3)
Fe2–N2	2.234(6)	2.235(5)	2.177(14)	2.208(3)
Fe1–O1	1.930(4)	1.931(5)	1.928(11)	1.923(2)
Fe2–O2	1.920(4)	1.934(5)	1.947(11)	1.939(2)
Fe1–O3	2.036(5)	2.024(4)	2.00(1)	2.008(2)
Fe2–O3	2.017(4)	2.019(4)	2.008(11)	2.013(2)
Fe1–Fe2	3.069	3.078	3.105(5)	3.058
Fe1-O3-Fe2	98.44	99.16	101.6(4)	99.04
O3-Fe1-O4	81.56	80.84	78.56	80.96
O3-Fe2-O4	81.56	80.84	78.15	80.96

[a] The numbering system follows Figure 2. Owing to the symmetry: Fe1–N1 = Fe2–N4; Fe1–N3 = Fe2–N2; Fe1–O1 = Fe2–O6; Fe1–O3 = Fe2–O4; Fe2–O3 = Fe1–O4; Fe1–O5 = Fe2–O2; O3-Fe1-O4 = O3-Fe2-O4 for **2b** and **2f**, and Fe1–N1 = Fe1–N3; Fe2–N2 = Fe2–N4; Fe1–O1 = Fe1–O5; Fe2–O2 = Fe2–O6; Fe1–O3 = Fe1–O4; Fe2–O3 = Fe2–O4 for **2e**.

is found in **2b**, the strands of the two ligand moieties are folded with twisting around two iron atoms to form a helical arrangement. As in **2b**, each iron atom has an octahedral geometry with N_2O_4-type hexacoordination. The whole molecule has C_2 symmetry, with the C_2 axis coincident with the Fe–Fe vector. As a result, the Fe_2O_2 rhombus has a mirror plane that involves two iron atoms.

The crystal structure of **2f** (Figure 4) is similar to that of **2b**, in that the strands of two ligand molecules are folded without twisting. The geometrical parameters and the coordination of N_2O_4 onto the iron atom were also quite similar to those of **2b**. The whole molecule has C_i symmetry, and the Fe_2O_2 rhombus has a point of symmetry.

Although there are differences in the manner of folding, that is, parallel or twisted, between **2b**, **2e**, and **2f**, their core parts are quite similar to each other, and can be illustrated as in Figure 2. The detailed geometrical parameters are summarized in Table 1. Those values are close to the typical values reported for $Fe^{III}{}_2(\mu\text{-}OR)_2$ complexes.[16] The

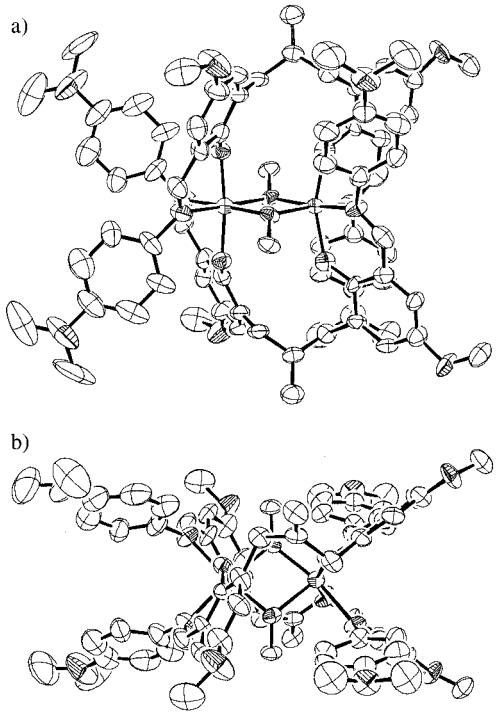

Figure 3. The crystal structure of **2e**. Views from the directions a) nearly parallel and b) nearly perpendicular to the Fe_2O_2 rhombic plane.

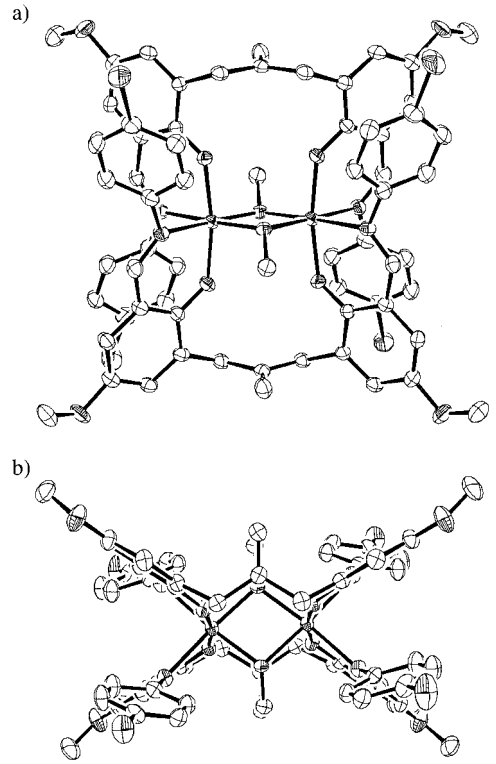

Figure 4. The crystal structure of **2f**. Views from the directions a) nearly parallel and b) nearly perpendicular to the Fe_2O_2 rhombic plane.

main features are: 1) the presence of four nitrogen atoms in the plane of the Fe_2O_2 rhombus and 2) the four phenolate groups lying out of the plane. Although one can logically think of such a geometry with a N_2O_4 core, only few examples are known in bis(μ-methoxo)diiron complexes. Because of this symmetry, the four phenolate groups and four phenylimine groups are virtually equivalent to one another; this significantly simplifies the interpretation of the redox behavior (see below). In view of the similarity of the ligands, the other complexes (**2a**, **2c**, **2d**, and **2g**) are presumed to have a similar structure to either **2b** or **2e**, with a rhombic core as shown in Figure 2.

Electrochemical properties: Cyclic voltammograms were measured for **2a**–**g**. As a typical example, the data for **2d** are shown in Figure 5. The solid line shows three reversible redox waves at −1.24, +0.43, and +0.59 V of $E_{1/2}$, which are designated as $E^{(1)}$, $E^{(2)}$, and $E^{(3)}$, respectively. Broadening the sweeping range to higher potentials (dashed line in Figure 5) resulted in the appearance of two additional

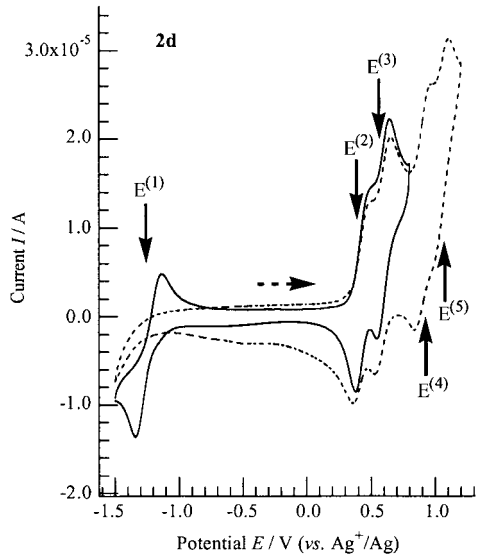

Figure 5. The cyclic voltammograms of **2d** with sweeping ranges of −1.5 to +0.8 V (solid line) and −1.5 to +1.2 V (dashed line). Half-wave potentials ($E^{(1)}$–$E^{(5)}$) are indicated by solid arrows. Initial potential −0.4 V, scan direction in oxidation (dashed arrow).

waves, observed at +0.96 and +1.11 V, which are indicated as $E^{(4)}$ and $E^{(5)}$, respectively, although they showed less clear reversibility. It is noteworthy that whereas all five waves are present upon starting scanning in the reduction direction, (initial potential = −0.4 V), the reduction wave $E^{(1)}$ is masked after the electrochemical cell has reached potentials as high as $E^{(5)}$, when starting scanning in oxidation.

For **2b**–**d** and **2f**, three redox waves at $E^{(1)}$, $E^{(2)}$, and $E^{(3)}$ were clearly observed when the sweeping range was chosen appropriately, although $E^{(1)}$ of **2b** was not reversible. The wave corresponding to $E^{(3)}$ was not observed for **2a**, **2e**, and **2g**. No clear cathodic wave for $E^{(2)}$ was observed for **2a**. For **2e** and **2g**, the redox wave at $E^{(2)}$ appeared to be a superposition of several peaks that were not well resolved. The $E_{1/2}$ values of those waves for **2a**–**g** are summarized in Table 2.

Table 2. Half-wave potentials of the redox waves [V]. Differences between anodic and cathodic peak potentials are in parenthesis.

	$E^{(1)}$	$E^{(2)}$	$E^{(3)}$
2a	−1.23 (0.20)	0.76[b]	–
2b	−1.30[a]	0.62 (0.10)	0.82 (0.10)
2c	−1.09 (0.23)	0.88 (0.10)	1.06 (0.10)
2d	−1.24 (0.20)	0.43 (0.10)	0.59 (0.10)
2e	−1.22 (0.21)	0.33 (0.1)[c]	–
2f	−1.17 (0.19)	0.49 (0.08)	0.66 (0.08)
2g	−1.20 (0.25)	0.52 (0.1)[c]	–

[a] Only a cathodic peak was observed. [b] Only an anodic peak was observed. [c] Values are less precise because of the low resolution of overlapped peaks.

The differences (ΔE_p) between anodic and cathodic potentials are also listed in Table 2. The ΔE_p values of $E^{(1)}$ (0.20–0.25 V) are over twice as large as those of $E^{(2)}$ and $E^{(3)}$ (0.08–0.10 V), suggesting that these redox waves originate from different reaction centers. Note that, as compared in Figure 6, the variation of $E^{(2)}$ and $E^{(3)}$ is much larger than that of $E^{(1)}$.

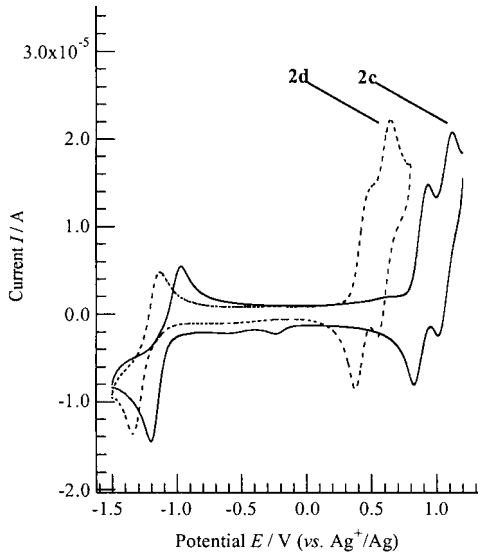

Figure 6. Comparison of the cyclic voltammograms of **2c** and **2d**.

The $E^{(1)}$ values range from −1.09 to −1.24 V, showing a difference of 0.15 V, depending on the substituent on the phenolate or phenylimine moieties. By comparison with the reported value,[13,16–20] the wave at $E^{(1)}$ can be assigned to the redox reaction of Fe^{III}/Fe^{II}. A clear high-potential shift observed for **2c** and **2f** is consistent with the stabilization of the Fe^{II} state through the introduction of an electron-withdrawing (chloro) group on the phenolate and phenylimine moieties, respectively. In the literature, some of the corresponding waves were observed as irreversible cathodic

peaks, assigned to reduction from $Fe^{III}Fe^{III}$ to $Fe^{II}Fe^{III}$,[17,19,20] and others were observed as two reversible and well-resolved waves.[13,16,18] In the present case, the wave at $E^{(1)}$ was single and reversible, and is attributable to the redox processes between $Fe^{III}Fe^{III}$ and $Fe^{III}Fe^{II}$.

Unlike the redox wave of Fe^{III}/Fe^{II}, the redox peaks at higher potentials have hardly been mentioned in the literature. In the present study, the half-wave potentials $E^{(2)}$ and $E^{(3)}$ varied depending on the substituent. By comparing these values with those for substituents on the phenol moiety (Table 2), we can straightforwardly reach a general rule: electron-donating groups on the phenol shift these peaks to the lower potential side, whereas electron-withdrawing groups shift them to the higher potential side. This strongly suggests that the peaks at $E^{(2)}$ and $E^{(3)}$ are related to the redox process of the phenolate moiety; however, the voltammogram of the isolated ligand **1d** showed a single, irreversible, anodic peak at 0.73 V (data not shown), which is almost at the center of the four redox waves of **2d**. In view of the direct link between the phenolate oxygen and the iron atom in **2a–g**, the redox process could be interpreted instead as a coupled redox process of the iron atoms and phenolate groups. In fact, in active sites of some iron-containing proteins in which phenoxy radicals are involved close to the metal,[1,2] the concomitant presence of both a tyrosylyl radical and an Fe^{IV}/Fe^{III} dinuclear center strongly suggests that both oxidation potentials of the tyrosine and Fe^{III} occur in similar range of potential.

Thus, we assume that the four redox waves ($E^{(2)}=0.43$, $E^{(3)}=0.59$, $E^{(4)}=0.96$, and $E^{(5)}=1.11$ V) observed for **2d** correspond to the four-electron oxidations of the four phenolate moieties. The splitting of the redox potential implies an electronic interference among four phenolate moieties, which were originally equivalent and should have shown a single redox wave. The differences in potential between $E^{(2)}$ and $E^{(3)}$ range from 0.14 to 0.20 V for **2b–d** and **2f**, and the difference between $E^{(4)}$ and $E^{(5)}$ for **2d** is 0.15 V, which also falls within this range. The narrowness of the range indicates that this value originates from an intrinsic property of the $Fe_2(\mu\text{-OMe})_2$ diamond core. In addition, the differences between $E^{(2)}$ and $E^{(4)}$, and between $E^{(3)}$ and $E^{(5)}$ are 0.53 and 0.52 V, respectively. This type of splitting can be qualitatively interpreted in terms of a simple model in which the highest occupied molecular orbitals ϕ_1–ϕ_4 of four phenolate groups are coupled through the $Fe_2(\mu\text{-MeO})_2$ core with three different coupling constants β_1–β_3 (Figure 7a), resulting in four combined molecular orbitals ψ_1–ψ_4 that have different orbital energies (Figure 7b). As β_1 is the interaction

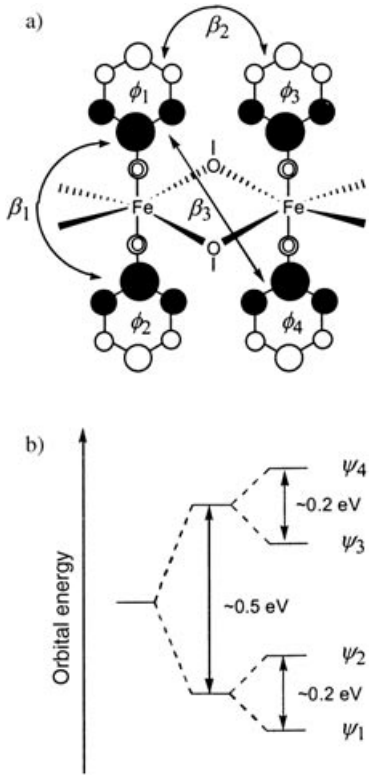

Figure 7. a) Schematic representation of the electronic interactions among HOMOs (ϕ_1–ϕ_4) of phenolate moieties. b) Splitting of the orbital energies of the molecular orbitals (ψ_1–ψ_4) that consist of HOMOs of phenolates.

passing through the -O–Fe–O- bonds, it is assumed to be much larger than β_2 and β_3, which are the interactions passing through the -O–Fe–(μ-OMe)$_2$–Fe–O- bonds. Therefore, β_1 contributes predominantly to the energy gap of ~0.5 eV, whereas β_2 and β_3 are responsible for the energy gap of ~0.2 eV. Conversely, these energy gap values could be a measure of the strength of the interactions.

From the viewpoint of organic electronic theory, this interaction arises from charge delocalization through resonance of the structure. We can consider the one-electron oxidation state of a bis(μ-methoxo)diiron complex as a hybrid of several resonance structures such as cationic phenoxyl radical or cationic Fe^{IV} complex (Scheme 2). Because of the existence of this resonance hybrid, the complex could achieve the $Fe^{III}Fe^{IV}$ mixed valence state. Based on this assumption, we should be able to observe the diiron complexes in the $Fe^{III}Fe^{IV}$ state resonating with the phenoxyl radical at a

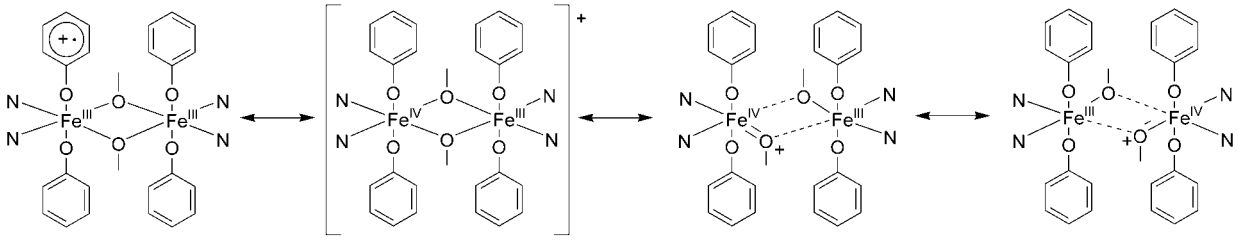

Scheme 2. Resonance structures of one-electron oxidized species of the diiron complex.

potential between $E^{(2)}$ and $E^{(3)}$. Similarly, at a potential between $E^{(3)}$ and $E^{(4)}$, the diiron complexes are in a resonating $Fe^{IV}Fe^{IV}$ state. We therefore believe that, in principle, the redox process of the phenolate moiety involves four steps, whereas complexes other than **2d** have ligands that are less electron-rich, so that only two steps for these are sufficiently reversible. In summary, the observed redox waves $E^{(1)}$–$E^{(3)}$ correspond to the reactions shown in Scheme 3.

The above model can also explain the difference between the voltammogram of **2g** and those of the others, for example, **2b** (Figure 8). The redox wave $E^{(2)}$ of **2g** was observed at 0.52 V as a single wave, whose peak current was about twice that of **2b**. Because of the rather broadened shape of the peaks, the redox waves corresponding to $E^{(2)}$ and $E^{(3)}$ were much closer to each other, so that they could not be resolved. Therefore, it is suggested that two naphtholate moieties are oxidized almost independently. Compared with phenolate, the naphtholate moiety has a large π-conjugated system that might be sufficient to stabilize the cationic radical without assistance from charge delocalization through the $Fe_2(\mu\text{-}MeO)_2$ core.

Provided that scheme 3 works appropriately, the $Fe_2(\mu\text{-}MeO)_2$ core could act as an electron mediator (or, more appropriately, a hole mediator), through which the redox states of phenolates interfer to some extent. The ability of the diiron core to act as a mediator may depend on the bridging units, such as μ-O, μ-OH, μ-OR, μ-RCO_2, and their combination; some of the bridging unit(s) might also involve a hydrogen bond. In other words, the bridging unit could be identified by observing the split width of the peaks of cyclic voltammograms. Further studies from this point of view will contribute to modeling and elucidating the catalytic mechanism of iron-containing enzymes.

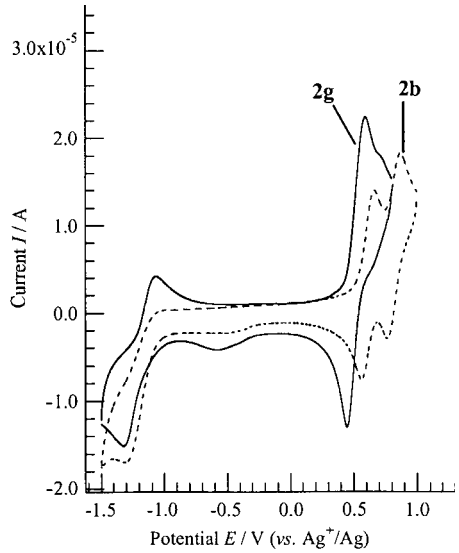

Figure 8. Comparison of the cyclic voltammograms of **2b** and **2g**.

Magnetic properties: The effective magnetic moments of the complexes were in the range 4.17–6.29 μ_B, which is much smaller than the value expected from the spin-only formula for two independent high-spin Fe^{III} atoms (8.37 μ_B).[30] Smaller magnetic susceptibility in bis(μ-methoxo)diiron complexes have been reported to arise from antiferromagnetic coupling interactions between the two iron atoms. The corresponding J values typically range from -8 to -11 cm^{-1}, leading to effective magnetic moment of 4.9–5.2 μ_B per iron center.[17] As the main purpose of this article is focused on electrochemistry, we have confined our study to room-temperature measurements.

Conclusion

Herein we have reported the first systematic study of the electrochemical behavior of bis(μ-methoxo)diiron complexes in the high-potential region. The Schiff base ligands that we previously developed formed bis(μ-methoxo)diiron complexes quite efficiently. We found two types of ligand

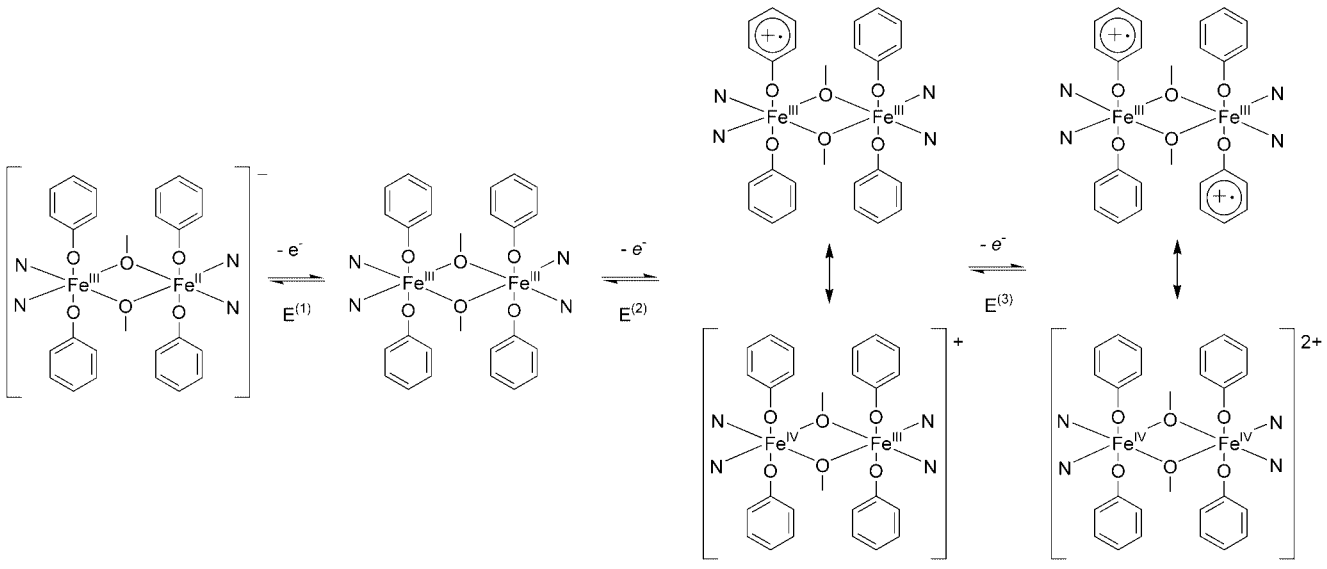

Scheme 3. Redox reactions of the diiron complex.

folding, that is, parallel and twisted, both of which have four phenolato groups sticking out of the Fe_2O_2 rhombic plane.

These complexes were sufficiently stable to allow us to study their electrochemical behavior at ambient temperature. The cyclic voltammetry measurements on these complexes revealed two or more distinct redox waves in a region of relatively high potential, in addition to known Fe^{III}/Fe^{II} redox waves in a lower potential region. We believe that these new peaks are related to the high-valence state of iron atoms, that is, $Fe^{III}Fe^{IV}$ and $Fe^{IV}Fe^{IV}$ states, resonating with the phenoxyl radical(s). The split widths of the redox waves certainly reflect the electronic interaction between face-to-face phenolate groups, mediated by the -O–Fe–(μ-OMe)$_2$–Fe–O- core. This finding implies that the Fe_2(μ-MeO)$_2$ core acts as an electron mediator (or, more appropriately, a hole mediator), with which the redox states of phenolates interfer to some extent.

Experimental Section

Ligands 1a–g: The Schiff base ligands **1a–g** were prepared by a reported procedure[22,23] and were characterized by ordinary analytical methods.

Synthesis of complexes 2a–g: A solution of iron (III) chloride hexahydrate (0.5 mmol) in methanol (25 mL) was added to a solution of **1** (0.5 mmol) in chloroform (25 mL). Triethylamine (1.5 mmol) was added to the mixture, which was stirred at 25 °C for 24 h. The reddish violet-to-black crystalline precipitate was collected by filtration, and washed with methanol.

Data for complex 2a: Reddish-violet solid; yield 75 %; elemental analysis (%) calcd for $C_{94}H_{118}N_4O_{10}Fe_2$: C 71.65, H 7.55, N 3.56; found: C 71.45, H 7.58, N, 3.43; ESI MS (+ mode): *m/z*: 1549.0 [M^+ −2 CH_3O+2 OH+H] (calcd: 1548.6); FT-IR (KBr): $\tilde{\nu}$ = 1612 (C=N), 1025 (CH_3O<), 831 cm^{-1} (Fe-O-Fe); μ_{eff}: 4.77 μ_B.

Data for complex 2b (*tert*-butyl derivative): Reddish-brown solid; yield 74 %; elemental analysis calcd (%) for $C_{82}H_{94}N_4O_{10}Fe_2 \cdot 0.5\,H_2O$: C 69.53, H 6.76, N 3.96; found: C 69.53, H 6.69, N 3.79; ESI MS (+ mode): *m/z*: 1375.7 [M^+ −CH_3O] (calcd: 1376.3); FT-IR (KBr): $\tilde{\nu}$ = 1614 (C=N), 1029 (CH_3O<), 840 cm^{-1} (Fe-O-Fe); μ_{eff}: 5.01 μ_B.

Data for complex 2c (chloro derivative): Brown solid; yield 83 %; elemental analysis calcd (%) for $C_{94}H_{114}N_4O_{10}Fe_2Cl_4$: C 65.89, H 6.71, N 3.27; found: C 65.67, H 6.60, N 3.04; ESI MS (+ mode): *m/z*: 1683.9 [M^+ −CH_3O] (calcd: 1682.4); FT-IR (KBr): $\tilde{\nu}$ = 1612 (C=N), 1027 (CH_3O<), 832 cm^{-1} (Fe-O-Fe); μ_{eff}: 6.29 μ_B.

Data for complex 2d (methoxy derivative): Brown solid; yield 94 %; elemental analysis calcd (%) for $C_{70}H_{70}N_4O_{14}Fe_2 \cdot 2\,H_2O$: C 62.78, H 5.57, N 4.19; found: C 62.78, H 5.06, N 3.96; ESI MS (+ mode): *m/z*: 1271.4 [M^+ −CH_3O] (calcd: 1272.0); FT-IR (KBr): $\tilde{\nu}$ = 1606 (C=N), 1034 (CH_3O<), 835 cm^{-1} (Fe-O-Fe); μ_{eff}: 5.01 μ_B.

Data for complex 2e (methoxydimethylamino derivative): Black solid; yield 74 %, recrystallized from dichloromethane; elemental analysis calcd (%) for $C_{74}H_{82}N_8O_{10}Fe_2 \cdot CH_2Cl_2$: C 62.55, H 5.88, N 7.78; found: C 62.67, H 5.81, N 7.54; ESI MS (+ mode): *m/z*: 1351.6 [M^+ −2 CH_3O+2 OH+ Na] (calcd: 1350.1); FT-IR (KBr): $\tilde{\nu}$ = 1608 (C=N), 1031 (CH_3O<), 828 cm^{-1} (Fe-O-Fe); μ_{eff}: 5.52 μ_B.

Data for complex 2f (methoxychloro derivative): Black solid; yield 58 %; elemental analysis calcd (%) for $C_{66}H_{58}N_4O_{10}Cl_4Fe_2 \cdot 2\,CHCl_3$: C 52.40, H 3.88, N 3.60; found: C 52.50, H 3.61, N 3.43; ESI MS (+ mode): *m/z*: 1292.9 [M^+ −2 CH_3O+2 OH+H] (calcd: 1294.1); FT-IR (KBr): 1597 (C=N), 1024 (CH_3O<), 833 cm^{-1} (Fe-O-Fe); μ_{eff}: 4.70 μ_B.

Data for complex 2g (naphthalene derivative): Brown solid; yield 71 %; elemental analysis calcd (%) for $C_{110}H_{126}N_4O_{10}Fe_2 \cdot H_2O$: C 73.65, H 7.19, N 3.12; found: C 73.56, H 7.10, N 2.96; ESI MS (+ mode): *m/z*: 1748.1 [M^+ −2 CH_3O+2 OH+H] (calcd: 1748.8); FT-IR (KBr): $\tilde{\nu}$ = 1611 (C=N), 1024 (CH_3O<), 828 cm^{-1} (Fe-O-Fe); μ_{eff}: 4.17 μ_B.

Electrochemical measurements: Electrochemical measurements were performed by using a conventional three-electrode cell with a glassy carbon working electrode, a platinum wire electrode, and an Ag^+/Ag reference electrode. The samples were prepared as 1.0 mM solutions in dichloromethane (anhydrous) with 0.1 M tetrabutylammonium hexafluorophosphate as the supporting electrolyte. Cyclic voltammograms were run by using a BAS model 400 electrochemical analysis system. Solutions were purged with nitrogen gas to remove oxygen before measurements were made. The values of the half-wave potential ($E_{1/2}$) were approximated by the average of anodic and cathodic peak potentials. Sweeps were started from the rest potential (about −0.4 V for the present system), with sweep rate of 100 $mV\,s^{-1}$, and the second and third scans were recorded. The initial direction was set as positive; measurements in the opposite direction gave essentially the same results for reversible systems. Although the sweep rate was varied from 50 to 1000 $mV\,s^{-1}$, no remarkable changes were observed for the reversibility of the voltammograms. All the measurements were made at 25 °C. For reference, the redox wave of ferrocene measured in these conditions occurred at 0.20 V of $E_{1/2}$ with 0.21 V of ΔE_p

Magnetic measurements: The magnetic moment was measured by Gouy's method, by using a Sherwood Scientific MSB-AUTO magnetic susceptibility balance. We assumed that the paramagnetic susceptibility (χ_P) arises from two iron atoms, and the diamagnetic component (χ_D) was estimated from ($0.5 \times 10^{-6} M$), whereby M is the molecular weight of the ligand moiety. The temperature-independent paramagnetic term was neglected. The effective magnetic moment (μ_{eff}) was given by $(8\chi_P T)^{1/2}$ in μ_B units, with a temperature (T) at the measurements of 298 K.

X-ray crystallography: For X-ray diffraction of single crystals, data were collected on a Rigaku RAXIS-RAPID imaging plate diffractometer with $\lambda(Mo_{K\alpha})$ = 0.7107 Å radiation. The structure was solved by direct methods and expanded by using Fourier techniques. The non-hydrogen atoms were refined anisotropically. The coordinates of hydrogen atoms were calculated. The final cycle of the full-matrix least-squares refinement was based on the observed reflections of $I > 1.5\sigma(I)$ and the variable parameters, and converged with unweighted and weighted agreement factors R_1 and R_w, respectively, as given below. All calculations were performed by using the Crystal Structure[28] crystallographic software package of the Molecular Structure Corporation. ORTEP drawings were made with ellipsoids of 50 % probability by using ORTEP-3 software.[29] In all the ORTEP figures, the hydrogen and solvent molecule atoms are omitted for clarity. CCDC-239204–239206 contain the supplementary crystallographic data for this paper. These data can be obtained free of charge via www.ccdc.cam.ac.uk/conts/retrieving.html (or from the Cambridge Crystallographic Data Center, 12 Union Road, Cambridge CB2 1EZ, UK; fax: (+44)1223–336–033; or deposit@ccdc.cam.ac.uk.

Crystal data for 2b: Black prisms recrystallized from dichloromethane; $C_{82}H_{94}Fe_2N_4O_{10} \cdot 2\,CH_2Cl_2$, M_r = 1577.22, triclinic, space group $P\bar{1}$(no.2), a = 14.129(8), b = 15.785(9), c = 20.834(7) Å, α = 106.50(2), β = 90.90(2), γ = 109.15(2)°, V = 4178.3(4) Å^3, Z = 2, T = 193 K, ρ_{calcd} = 1.254 $g\,cm^{-3}$, $\mu(Mo_{K\alpha})$ = 5.32 cm^{-1}, 40251 reflections measured and 9321 unique ($2\theta_{max}$ = 55.0°, R_{int} = 0.095), which were all used in the calculations; R = 0.081, R_w = 0.094.

Crystal data for 2e: Black prisms as precipitated; $C_{74}H_{82}Fe_2N_8O_{10}$, M_r = 1355.20, monoclinic, space group $C2/c$ (no.15), a = 22.77(1), b = 19.14(1), c = 16.807(9) Å, β = 97.82(5)°, V = 7255.5(7) Å^3, Z = 4, T = 193 K, ρ_{calcd} = 1.241 $g\,cm^{-3}$, $\mu(Mo_{K\alpha})$ = 4.61 cm^{-1}, 17288 reflections measured and 2132 unique ($2\theta_{max}$ = 55.0°, R_{int} = 0.166), which were all used in the calculations; R = 0.092, R_w = 0.129.

Crystal data for 2f: Black prisms as precipitated; $C_{33}H_{29}Cl_5Fe_2N_2O_5 \cdot CHCl_3$, M_r = 779.73, triclinic, space group $P\bar{1}$ (no.2), a = 10.323(4), b = 13.186(5), c = 13.573(5) Å, α = 94.49(3), β = 110.82(3), γ = 92.64(3)°, V = 1716.3(1) Å^3, Z = 2, T = 193 K, ρ_{calcd} = 1.509 $g\,cm^{-3}$, $\mu(Mo_{K\alpha})$ = 8.72 cm^{-1}, 15869 reflections measured and 4553 unique ($2\theta_{max}$ = 55.0°, R_{int} = 0.045), which were all used in the calculations; R = 0.047, R_w = 0.080.

[1] M. Merkx, D. A. Kopp, M. H. Sazinsky, J. L. Blazyk, J. Müller, S. J. Lippard, *Angew. Chem.* **2001**, *113*, 2860–2888; *Angew. Chem. Int. Ed.* **2001**, *40*, 2782–2807.

[2] L. Que, Jr., W. B. Tolman, *Angew. Chem.* **2002**, *114*, 1160–1185; *Angew. Chem. Int. Ed.* **2002**, *41*, 1114–1137.
[3] H.-F. Hsu, Y. Dong, L. Shu, V. G. Young, Jr., L. Que, Jr., *J. Am. Chem. Soc.* **1999**, *121*, 5230–5237.
[4] V. L. MacMurdo, H. Zheng, L. Que, Jr., *Inorg. Chem.* **2000**, *39*, 2254–2255.
[5] H. Zheng, S. J. Yoo, E. Münck, L. Que, Jr., *J. Am. Chem. Soc.* **2000**, *122*, 3789–3790.
[6] M. Costas, J.-U. Rohde, A. Stubna, R. Y. N. Ho, L. Quaroni, E. Münck, L. Que, Jr., *J. Am. Chem. Soc.* **2001**, *123*, 12931–12932.
[7] A. J. Skulan, M. A. Hanson, H.-F. Hsu, L. Que, Jr., E. I. Solomon, *J. Am. Chem. Soc.* **2003**, *125*, 7344–7356.
[8] D. Lee, J. D. Bois, D. Petasis, M. P. Hendrich, C. Krebs, B. H. Huynh, S. J. Lippard, *J. Am. Chem. Soc.* **1999**, *121*, 9893–9894.
[9] S. Kiani, A. Tapper, R. J. Staples, P. Stavropoulos, *J. Am. Chem. Soc.* **2000**, *122*, 7503–7517.
[10] T. Lovell, W.-G. Han, T. Liu, L. Noodleman, *J. Am. Chem. Soc.* **2002**, *124*, 5890–5894.
[11] W.-G. Han, T. Lovell, T. Liu, L. Noodleman, *Inorg. Chem.* **2003**, *42*, 2751–2758.
[12] L. Borer, L. Thalken, C. Ceccarelli, M. Glick, J. H. Zhang, W. M. Reiff, *Inorg. Chem.* **1983**, *22*, 1719–1724.
[13] S. K. Dutta, K. K. Nanda, U. Flörke, M. Bhadbhade, K. Nag, *J. Chem. Soc. Dalton Trans.* **1996**, 2371–2379.
[14] R. K. Egdal, A. Hazell, F. B. Larsen, C. J. McKenzie, R. C. Scarrow, *J. Am. Chem. Soc.* **2003**, *125*, 32–33.
[15] P. Baran, A. Böttcher, H. Elias, W. Hesse, M. Hüber, H. Fuess, H. Paulus, *Z. Naturforsch. Teil B* **1992**, *47*, 1681–1686.
[16] B. S. Snyder, G. S. Patterson, A. J. Abrahamson, R. H. Holm, *J. Am. Chem. Soc.* **1989**, *111*, 5214–5223.
[17] R. Viswanathan, M. Palaniandavar, P. Prabakaran, P. T. Muthiah, *Inorg. Chem.* **1998**, *37*, 3881–3884.
[18] H. Aneetha, K. Panneerselvam, T.-F. Liao, T.-H. Lu, C.-S. Chung, *J. Chem. Soc. Dalton Trans.* **1999**, 2689–2694.
[19] S. Negoro, H. Asada, M. Fujiwara, T. Matsushita, *Inorg. Chem. Commun.* **2003**, *6*, 357–360.
[20] M. Scarpellini, A. Neves, A. J. Bortoluzzi, I. Vencato, V. Drago, W. A. Ortiz, C. Zucco, *J. Chem. Soc. Dalton Trans.* **2001**, 2616–2623.
[21] M. Mikuriya, Y. Kakuta, R. Nukada, T. Kotera, T. Tokii, *Bull. Chem. Soc. Jpn.* **2001**, *74*, 1425–1434.
[22] H. Houjou, S. Tsuzuki, Y. Nagawa, K. Hiratani, *Bull. Chem. Soc. Jpn.* **2002**, *75*, 831–839.
[23] H. Houjou, S. Tsuzuki, Y. Nagawa, M. Kanesato K. Hiratani, *Bull. Chem. Soc. Jpn.* **2003**, *76*, 2405–2411.
[24] M. L. N. Rao, H. Houjou, K. Hiratani, *Chem. Commun.* **2002**, 420–421.
[25] M. Kanesato, H. Houjou, Y. Nagawa, K. Hiratani, *Inorg. Chem. Commun.* **2002**, *5*, 984–988.
[26] H. Houjou, A. Iwasaki, T. Ogihara, M. Kanesato, S. Akabori, K. Hiratani, *New J. Chem.* **2003**, *27*, 886–889.
[27] P. Ghosh, E. Bill, T. Weyhermuller, K. Wieghardt, *J. Am. Chem. Soc.* **2003**, *125*, 3967–3979.
[28] Crystal Structure Version 3.10: Rigaku Corporation and Rigaku/MSC, Tokyo, Japan, **2002**.
[29] ORTEP-3 for Windows: L. J. Farrugia, *J. Appl. Crystallogr.* **1997**, *30*, 565.
[30] For two independent spins in the same molecule, the total magnetic moment is square root of $4S_1(S_1+1)+4S_2(S_2+1)$. If $S_1=S_2=5/2$, that becomes 8.37 μ_B.

Received: February 5, 2004
Published online: August 2, 2004

